Open access

Superior tensile properties of 1%C-CoCrFeMnNi high-entropy alloy additively manufactured by selective laser melting

Jeong Min Park[a], Jungho Choe[b], Jung Gi Kim [a,c], Jae Wung Bae[a], Jongun Moon[a], Sangsun Yang[b], Kyung Tae Kim[b], Ji-Hun Yu[b,d], and Hyoung Seop Kim [a]

[a] Department of Materials Science and Engineering, Pohang University of Science and Technology, Pohang, Republic of Korea [b] Powder & Ceramic Division, Korea Institute of Materials Science (KIMS), Changwon, Republic of Korea [c] Max-Planck-Institut für Eisenforschung GmbH, Düsseldorf, Germany [d] Metal 3D Printing Convergence Research Team, Korean Institute of Machinery & Materials (KIMM), Daejeon, Republic of Korea

ABSTRACT

CoCrFeMnNi high-entropy alloys containing 1 at% carbon (C-HEAs) were additively manufactured using selective laser melting (SLM). Superior tensile properties of the as-built C-HEA (to previously reported ones) were achieved by utilizing multiple strengthening mechanisms (i.e. solid solution, grain refinement, dislocation density, and nano-precipitation) by this new manufacturing method. In particular, the SLM process could allow to maximize the strengthening effect of carbon addition to HEAs via finely distributed nano-carbides at the boundaries of solidification cellular structure. This work will open a new window to utilize the SLM process for enhanced mechanical properties of HEAs with great potential.
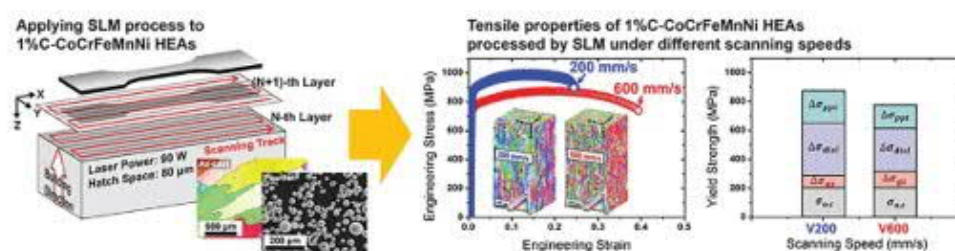
IMPACT STATEMENT

CoCrFeMnNi high-entropy alloys containing 1 at% carbon were successfully produced by selective laser melting, and the alloys exhibited much better tensile performance than additive manufactured high-entropy alloy previously reported.

CONTACT Hyoung Seop Kim ✉ hskim@postech.ac.kr ▣ Department of Materials Science and Engineering, Pohang University of Science and Technology, Pohang 37673, Republic of Korea

Introduction

High-entropy alloys (HEAs) are defined as alloys containing multi-principal elements with high configurational entropy [1]. Among them, the face-centered cubic (FCC) HEAs (typically, Cantor alloy: CoCrFeMnNi [2]) have been extensively studied due to their outstanding mechanical performance (e.g. excellent fracture toughness [3], cryogenic properties [4], and high ballistic resistance [5]). However, for engineering applications, FCC HEAs often exhibit a critical drawback: insufficient yield strength, while their ductility is superfluous. To overcome these drawbacks, obtaining both high yield-strength and reasonable ductility of HEAs has been attempted using precipitation hardening [6] or multi-phase structure [7,8]. In particular, it was suggested that the addition of a small amount of interstitial atoms (e.g. carbon) to FCC HEAs could effectively enhance their yield strength [9].

In contrast, applying novel processes to HEAs might reveal a favorable approach for enhancing their mechanical properties. In particular, additive manufacturing using selective laser melting (SLM) has great potential to obtain not only products of complex shapes but also HEAs of superior mechanical properties [10]. Using this process, three-dimensional (3D) products can be directly fabricated using high-energy laser beams to fuse layer-upon-layer of metallic powders [11]. This can enhance the design freedom using topology optimization for better service performance of the metallic components. Furthermore, recent studies reported that SLM-processed metallic materials showed a combination of improved strength and ductility due to severely heterogeneous microstructure [10–13]. In this study, C-containing CoCrFeMnNi HEAs (C-HEAs) were successfully fabricated using the SLM process. Detailed investigation of the strengthening effects afforded by the SLM process was performed in parallel with microstructural analyses.

Materials and methods

As the raw materials, the $(CoCrFeMnNi)_{99}C_1$ (at%) powder was prepared using gas atomization from vacuum induction melted ingots to obtain spherical powder particles for the SLM process (detailed information of the powder is in the supplementary with Supplementary Figs. S1 and S2, and Table S1). During the SLM process, rectangular samples $(30 \times 6 \times 6\ mm^3)$ were built with a 90 W laser, with hatch space of 80 μm, and layer thickness of 25 μm, using a commercial SLM machine (Mlab, Concept Laser Ltd.). This was done at two different laser scanning-speed conditions: 200 and 600 mm s^{-1} (labeled C-HEA-V200 and C-HEA-V600 in this paper). The scanning direction rotates 180° between (N)th and (N + 1)th layers with raster scanning patterns, and tensile specimens having a dog-bone-shape (gauge length 5.0 mm, width 2.5 mm, thickness 1.5 mm) were made from the as-built samples, as shown in Figure 1(a). The tensile tests were conducted at a strain rate of $10^{-3}\ s^{-1}$ using a universal testing machine (Instron 1361) with the digital image correlation technique using ARAMIS 5M at room temperature. All tensile tests were repeated at least three times.
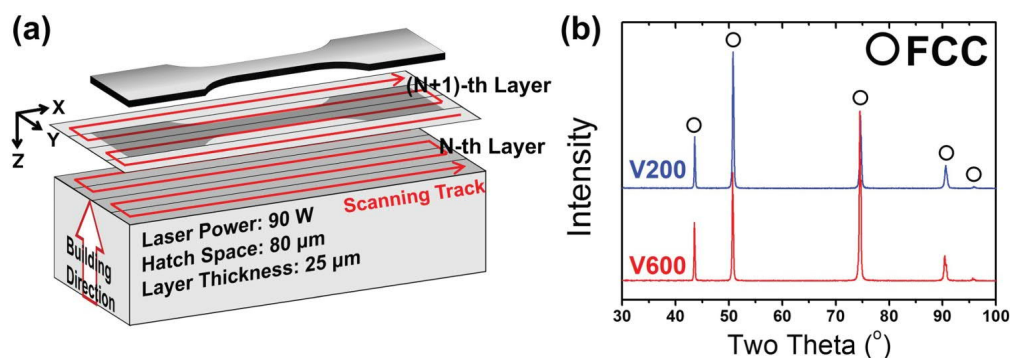

Figure 1. (a) Schematic of the SLM scanning strategy and (b) XRD patterns of the as-built C-HEAs.

For microstructural characterization, all the specimens were mechanically polished to a surface roughness of 1 µm, followed by colloidal silica polishing. Then, X-ray diffraction (XRD) was carried out using RIGAKU D/MAX-2500 with Cu Kα radiation, as shown in Figure 1(b), which indicates a single FCC structure of as-built C-HEAs. Electron backscatter diffraction (EBSD) analysis was also performed using a field emission scanning electron microscope (FE-SEM, XL-30S FEG, FEI Co.) equipped with an energy-dispersive X-ray spectroscopy (EDS) detector. Elemental analysis of the samples was conducted using an EDS and Carbon/Sulfur determinator (CS-844, LECO Co.). Furthermore, transmission electron microscope (TEM, JEM-2200FS, JEOL Ltd.) analysis was performed equipped with an electron energy loss spectroscopy (EELS) detector for the specimens extracted by a site-specific technique using a focused ion beam (FIB, FEI Co.).

Results and discussion

Figure 2 indicates the EBSD maps and SEM-backscatter electron (BSE) images of the as-built C-HEAs. The high angle grain boundaries (HAGBs, misorientation angles > 15°) are indicated by black lines in the EBSD maps. As shown in the 3D inverse pole figure (IPF) maps (Figure 2(a,d)), the as-built samples exhibited unique microstructure due to characteristics of the SLM process: the grains on the building plane (Z plane) were arrayed along the laser-scanning track with rectangular shape, while the columnar grain structure was observed along the building (Z) direction on the lateral surface of both samples. In the present SLM process, the laser-beam passed continuously along the X direction on the building plane of the sample, which led to the formation of a linear arrangement of grains along the scanning tracks with repeated rapid melting and cooling. The heat flux at the (N + 1)th layer was directly transferred through the Nth layer, with the formation of a columnar grain structure, by epitaxial solidification along the side opposite to the building direction [10]. Meanwhile, the average grain size on the Z plane of the C-HEA-V200 (~35.5 µm) was much larger than that of the C-HEA-V600 (~20.3 µm). This is attributable to a difference in the heat input during the SLM process at different scanning speeds [12]. The lower scanning speed led to higher energy input due to a longer time of exposure to the laser beam. The volumetric energy density (E_v) from laser scanning for the SLM process can be estimated using the following equation [12]:

$$E_v = P/(v \cdot h \cdot \Delta l) \tag{1}$$

where P is the laser power, v is the scanning speed, h is the hatch distance, and Δl is the layer thickness of the SLM process. The calculated energy inputs to the V200 and V600 samples become ~225 and 75 J mm^{-3}, respectively: the value of the V200 sample is three times higher than that of the V600 sample. The results of elemental analysis of the C-HEA samples are presented in Table 1. This demonstrates that the manganese evaporation was more severe in the C-HEA-V200 due to the higher heat input during the SLM process. Figure 2(b,e) show kernel average misorientation (KAM) maps of the C-HEA-V200 and -V600 samples (for KAM distribution profiles, see Supplementary Fig. S3), which revealed higher KAM value distributions than for fully recrystallized alloys [8]. In most cases, the SLM-processed materials involve high dislocation density and thermal residual stress due to the complex thermal history of a process with a rapid-cooling rate (~10^6 K/s) [10–14], which is usually related to the solidification substructure (e.g. cellular structure) as shown in Figure 2(c,f). Interestingly, the C-HEA-V200 showed more fraction of low angle grain boundaries (LAGBs, misorientation angles < 15°) than did the C-HEA-V600 (see Supplementary Table S2). It is expected that the increased scanning speed of the SLM process could lead to decreased thermal residual stress for present the HEAs [14–17].
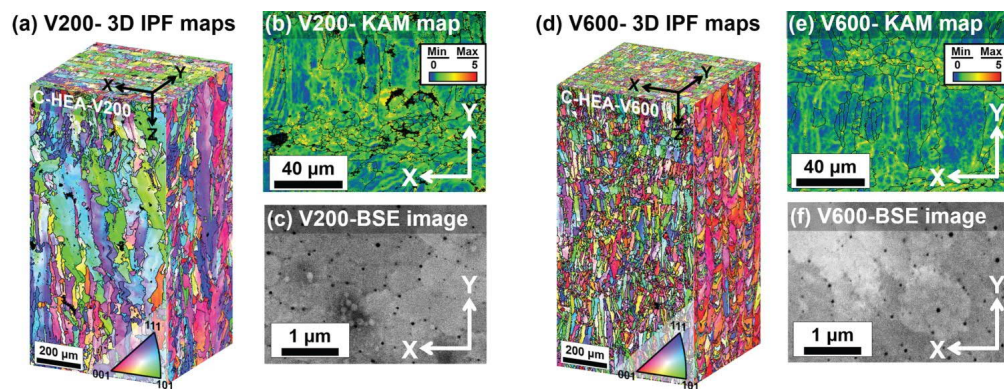
_____   _____

Figure 2. Microstructure of the (a–c) C-HEA-V200 and (d–f) C-HEA-V600: (a, d) inverse pole figure (IPF) maps, (b, d) kernel average misorientation (KAM) maps, and (c, f) SEM-BSE images.

Table 1. Chemical compositions of the as-cast and SLM-processed C-HEAs. (Table view)

Samples	Chemical compositions, at%						
	Co	Cr	Fe	Mn	Ni	C	S
As-Cast	19.81	19.36	19.79	19.65	20.36	1.02	0.01
V200	20.49	20.61	20.45	16.68	20.85	0.89	0.03
V600	20.24	20.51	20.24	17.40	20.61	0.97	0.03

Meanwhile, as indicated in high-magnification BSE images of the samples, nano-precipitates were obviously detected along the boundaries of the cellular structure (Figure 2(c,f)). Figure 3 shows TEM micrographs of the C-HEA-V200 sample (for the C-HEA-V600, see Supplementary Fig. S4). As shown in Figure 3(a,b), the boundaries of the cellular sub-grains were decorated with highly entangled dislocations related to high residual stress of the SLM-produced samples [10–14]. Furthermore, the STEM image (Figure 3(c)) clearly presents a number of nano-precipitates with nearly spherical shape (highlighted by yellow arrows). To clarify these precipitates in the as-built samples, elemental analysis was carried out using the EELS mappings, as indicated in Figure 3(d). This clearly indicates that the precipitates are a mixture of Mn-rich oxide and sulfide, and of Cr-rich carbide with size in the range 30–70 nm. For the C-HEA-V200 and C-HEA-V600 samples, the measured volume fractions of the precipitates were ∼1.73% and ∼1.13%, respectively, based on 2D image analysis for their microstructures. It is noteworthy that the C-HEA-V200 had a higher volume fraction of nano-precipitates than the C-HEA-V600 had. The precipitation of the Cr-rich carbide has usually been reported for alloys having high Cr content (e.g. stainless steel) during the welding process, with exposure to a specific temperature range (approximately 400–800°C), which is generally called sensitization [18–20]. This usually results from the rapid diffusion of elemental Cr (with high affinity for interstitial carbon) to the grain boundaries of the alloy with the formation of Cr-rich $M_{23}C_6$ carbides [20]. In addition, during the welding process, the higher heat input often leads to a slower cooling rate, which accommodates longer exposure time of the sensitization temperature, which increases the amount of carbides in the alloy [18–20]. Zhou et al. [21] investigated the precipitation behavior of CoCrFeNi HEAs containing 1.2 at% carbon, which were fabricated using SLM. They reported that the precipitation of nano-scale $Cr_{23}C_6$-type carbide occurred after annealing heat treatment at 800°C. Furthermore, they reported that the volume fraction of carbides in the alloy increased with increasing annealing time [21]. Similarly, by repeated heating and cooling during the SLM process, the alloy could also frequently be exposed to the temperature range of Cr-rich carbide formation, and the slower laser scanning might lead to longer exposure time for carbide formation.
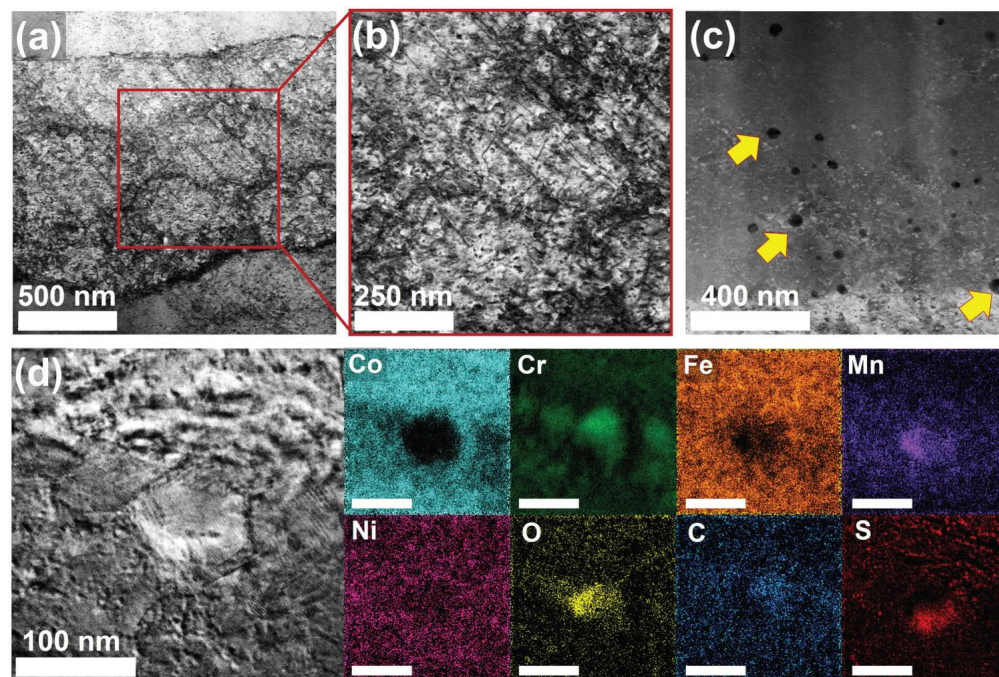
Figure 3. TEM micrographs of the SLM-processed C-HEA at the scanning speed of 200 mm s^{-1}: (a) bright-field image of cellular structures, (b) magnified image, (c) STEM image indicating the presence of nano-precipitates, and (d) EELS mapping images of both substitutional (Co, Cr, Fe, Mn, and Ni) and interstitial (O, C, and S) elements for the nano-precipitates (right side).

The tensile properties of the samples are displayed in Figure 4(a). It was noted that the SLM-processed samples showed drastic enhancement of yield strength as compared with the as-cast C-HEA. Furthermore, the as-built 1%C-CoCrFeMnNi HEAs exhibited considerably higher strength levels than those of CoCrFeMnNi HEAs (labeled HEA-V200 and -V600) in this works (detailed information of as-built CoCrFeMnNi HEAs is in the supplementary information with Supplementary Fig. S5 and Table S3). It demonstrates that the addition of a small amount of carbon contributed to effectively enhance mechanical properties of SLM-processed HEAs, while it could have a less effect on strengthening of as-cast HEAs [9]. Moreover, the SLM-processed HEAs in this works presented much better performance than did the other SLM-processed HEAs as shown in Figure 4(b). This novel improvement of mechanical properties for current samples could be attributed to the optimized combination of various strengthening mechanisms for high yield strength, and hierarchically heterogeneous microstructure for reasonable ductility [10,22].
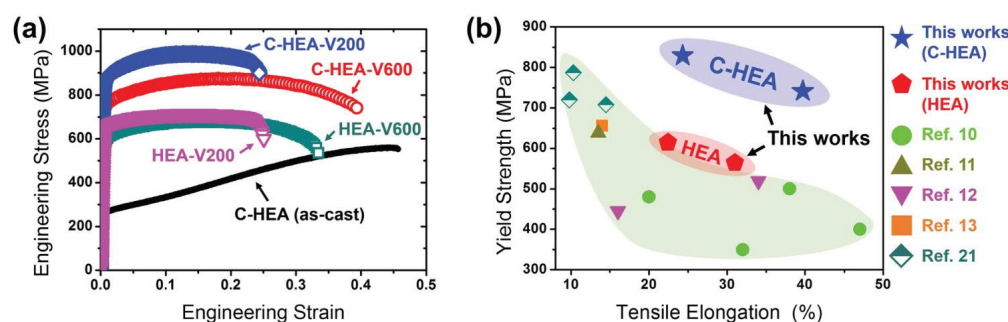

Figure 4. (a) Tensile properties of the as-cast and as-built samples. (b) Comparison of the yield strength vs. tensile elongation obtained in our work, with other SLM-processed Co–Co–Fe–Mn–Ni HEAs.

The C-HEA-V200 exhibited extremely high yield and tensile strengths (~829 and ~989 MPa, respectively), along with a reasonable total elongation of ~24.3%. For the C-HEA-V600, it is noted that

the samples also exhibited high yield strength of ∼741 MPa and tensile strength of ∼874 MPa, whereas total elongation (∼39.7%) was slightly decreased as compared with that of the as-cast samples (∼45.7%). Interestingly, the C-HEA-V200 were much stronger than the C-HEA-V600, although the C-HEA-V200 sample had a larger grain size.

To explore this tendency, the major strengthening mechanisms for the SLM-processed C-HEAs were considered to be the combination of dislocation hardening, grain refinement, and precipitation hardening [21]. This was simplified in the following equation:

$$\sigma_{YS} = \sigma_{o,c} + \Delta\sigma_{gb} + \Delta\sigma_{disl} + \Delta\sigma_{ppt} \tag{2}$$

where σ_{YS} is the yield strength of the as-built samples, and $\Delta\sigma_{gb}$, $\Delta\sigma_{disl}$, and $\Delta\sigma_{ppt}$ are the strengthening contributions made by grain boundary, dislocation, and precipitation, respectively. The lattice frictional strength of the present alloy, $\sigma_{o,c}$, can be considered a summation of the friction stress of the CoCrFeMnNi HEA (σ_o = ∼125 MPa [23]) and interstitial solid solution effect of carbon (σ_c). From the Hall–Petch relationship, the $\Delta\sigma_{gb}$ can be regarded as $K \cdot d^{-1/2}$, where d is the average grain size, and K is a grain boundary strengthening coefficient (∼494 MPa μm$^{-1/2}$ in the CoCrFeMnNi HEA [23]). In the C-HEA-V200 and -V600 samples, $\Delta\sigma_{gb}$ could be estimated to be ∼82 and ∼109 MPa, respectively. Based on these estimates, the interstitial solid solution effect (σ_c) by carbon content could be calculated using the average grain size of the as-cast samples (∼800 μm). The estimated value of σ_c was ∼78 MPa, which is almost the same as the effect of carbon interstitial strengthening on austenitic steel (∼77 MPa/at% [24]). In addition to this, the $\sigma_{o,c}$ of the present alloy was ∼203 MPa.

In most cases, the high dislocation density has a key effect on the high strength level in SLM-processed materials [11,22]. For the dislocation hardening effect, the following Taylor equation can be applied [25]:

$$\Delta\sigma_{disl} = M\alpha Gb\rho^{1/2} \tag{3}$$

where M is the Taylor factor (3.06 for FCC materials), α is a constant (0.2 for FCC materials [25]), G is the shear modulus (∼81 GPa [26]), b is the Burgers vector (estimated to be ∼0.254 nm from the XRD patterns in Figure 1(d)), and ρ is the dislocation density. To determine the dislocation density of as-built samples, a convolutional multiple whole profile (CMWP) analysis was conducted using XRD patterns (Figure 1(d)) with the peak of LaB6 powder as a reference [27]. The measured values of ρ were ∼8.5 and ∼5.8 × 10^{14} m^{-2} for the C-HEA-V200 and -V600 samples, respectively. It should be noted that these dislocation density values are much higher than those in the as-cast or sintered HEAs [25]. From these data, the $\Delta\sigma_{disl}$ values of the C-HEA-V200 and -V600 samples could be estimated to be ∼367 and ∼303 MPa, respectively.

The contribution of precipitation hardening by the Orowan mechanism can be expressed as [21,25]

$$\Delta\sigma_{ppt} = M\frac{0.4Gb}{\pi\lambda}\frac{\ln(2\bar{r}/b)}{\sqrt{1-v}} \tag{4}$$

$$\lambda = 2\bar{r}\left(\sqrt{\frac{\pi}{4f}} - 1\right) \tag{5}$$

$$\bar{r} = r\sqrt{2/3} \tag{6}$$

where v is Poisson's ratio (0.265 [25]), λ is the edge-to-edge inter-precipitates spacing, r is the mean precipitate radius (∼22.48 and 24.32 nm for C-HEA-V200 and -V600), $\bar{r}$ is the mean radius of a circular

cross section in a random plane, and f is the volume fraction of the precipitate. By calculating Equations (4)–(6), the predicted values of $\Delta\sigma_p$ were ~201 and ~161 MPa for the C-HEA-V200 and -V600, respectively. As shown in Figure 5, by substituting each strengthening contribution to Equation (2), the predicted yield strengths become ~873 and ~777 MPa for the C-HEA-V200 and -V600, which exhibit good agreement with our experimental data.
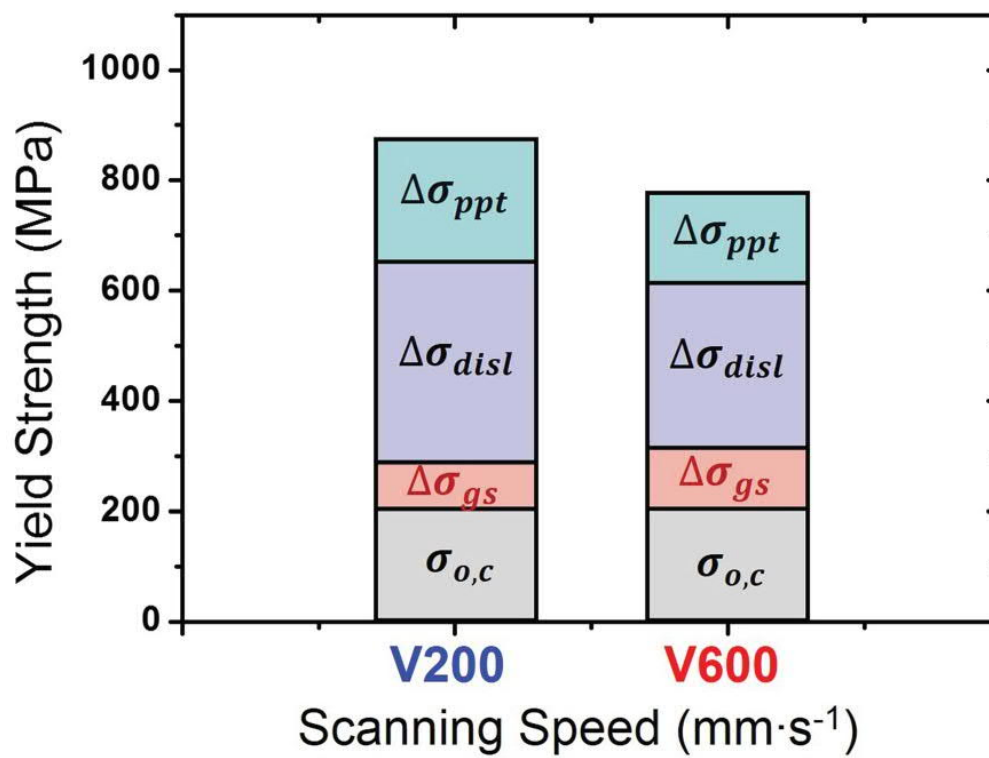

Figure 5. Strength contributions from different strengthening mechanisms of SLM-processed C-HEAs in different scanning speed conditions.

Conclusions

In this study, CoCrFeMnNi HEAs with the minor addition of carbon (~1 at%) were excellently fabricated using the SLM process at scanning speeds of 200 and 600 mm s^{-1}. The alloys exhibited significant improvement of tensile properties after the SLM process as compared with as-cast conditions. This outstanding performance of the alloys could be attributed to their complex microstructure with a combination of various strengthening mechanisms. In particular, the addition of carbon in this work appeared to have a substantial effect on the strength enhancement of SLM-processed CoCrFeMnNi HEAs via not only interstitial solid solution but also precipitation hardening. In addition, the samples built at different scanning speeds exhibited different levels of strength, as explored by comparing each strengthening contribution. The results implied that different energy input might be a major factor that could lead to the creation of varying microstructure with disparate contributions to strengthening. This demonstrates that our work can offer additional guidelines for optimizing the SLM process to develop the novel performance of HEAs.

Disclosure statement

Funding

Processes for Metal 3D Printing (PNK5520)' of the Korea Institute of Materials Science (KIMS), and by the Creative Materials Discovery Program of the National Research Foundation of Korea (NRF) funded by the Ministry of Science and ICT (NRF-2016M3D1A1023384).

References

[1] Miracle DB. High entropy alloys as a bold step forward in alloy development. *Nat Commun*. 2019;10:1805. Crossref. PubMed.

[2] Cantor B, Chang ITH, Knight P, et al. Microstructure development in equiatomic multicomponent alloys. *Mater Sci Eng A*. 2004;375–377:213–218. Crossref.

[3] Gludovatz B, Hohenwarter A, Catoor D, et al. A fracture-resistant high-entropy alloy for cryogenic applications. *Science*. 2014;345:1153–1158. Crossref. PubMed.

[4] Jang MJ, Kwak H, Lee YW, et al. Plastic deformation behavior of 40Fe-25Ni-15Cr-10Co-10V high-entropy alloy for cryogenic applications. *Met Mater Int*. 2019;25:277–284. Crossref.

[5] Li Z, Zhao S, Alotaibi SM, et al. Adiabatic shear localization in the CrMnFeCoNi high-entropy alloy. *Acta Mater.* 2018;151:424–431. Crossref.

[6] Ming K, Bi X, Wang J. Precipitation strengthening of ductile $Cr_{15}Fe_{20}Co_{35}Ni_{20}Mo_{10}$ alloys. *Scr Mater.* 2017;137:88–93. Crossref.

[7] Park JM, Moon J, Bae JW, et al. Effect of annealing heat treatment on microstructural evolution and tensile behavior of $Al_{0.5}$CoCrFeMnNi high-entropy alloy. *Mater Sci Eng A*. 2018;728:251–258. Crossref.

[8] Park JM, Moon J, Bae JW, et al. Role of BCC phase on tensile behavior of dual-phase $Al_{0.5}$CoCrFeMnNi high-entropy alloy at cryogenic temperature. *Mater Sci Eng A*. 2019;746:443–447. Crossref.

[9] Li Z. Interstitial equiatomic CoCrFeMnNi high-entropy alloys: carbon content, microstructure, and compositional homogeneity effects on deformation behavior. *Acta Mater.* 2019;164:400–412. Crossref.

[10] Zhu ZG, Nguyen QB, Ng FL, et al. Hierarchical microstructure and strengthening mechanisms of a CoCrFeNiMn high entropy alloy additively manufactured by selective laser melting. *Scr Mater.* 2018;154:20–24. Crossref.

[11] Wu W, Zhou R, Wei B, et al. Nanosized precipitates and dislocation networks reinforced C-containing CoCrFeNi high-entropy alloy fabricated by selective laser melting. *Mater Charact*. 2018;144:605–610. Crossref.

[12] Li R, Niu P, Yuan T, et al. Selective laser melting of an equiatomic CoCrFeMnNi high-entropy alloy: processability, non-equilibrium microstructure and mechanical property. *J Alloys Compd*. 2018;746:125–134. Crossref.

[13] Zhou R, Liu Y, Zhou C, et al. Microstructures and mechanical properties of C-containing FeCoCrNi high-entropy alloy fabricated by selective laser melting. *Intermetallics*. 2018;94:165–171. Crossref.

[14] Liu Y, Yang Y, Wang D. A study on the residual stress during selective laser melting (SLM) of metallic powder. *Int J Adv Manuf Technol*. 2016;87:647–656. Crossref.

[15] Kong F, Ma J, Kovacevic R. Numerical and experimental study of thermally induced residual stress in the hybrid laser-GMA welding process. *J Mater Process Technol*. 2011;211:1102–1111. Crossref.

[16] Teng TL, Lin CC. Effect of welding conditions on residual stresses due to but welds. *Int J Pres Ves Pip*. 1998;75:857–864. Crossref.

[17] Anawa EM, Olabi AG. Control of welding residual stress for dissimilar laser welded materials. *J Mater Process Technol*. 2008;204:22–33. Crossref.

[18] Mohammed GR, Ishak M, Aqida SN, et al. Effects of heat input on microstructure, corrosion and mechanical characteristics of welded austenitic and duplex stainless steels: a review. *Metals (Basel)*. 2017;7:39. Crossref.

[19] Lee HT, Wu JL. Correlation between corrosion resistance properties and thermal cycles experienced by gas tungsten arc welding and laser beam welding alloy 690 butt weldments. *Corros Sci*. 2009;51:733–743. Crossref.

[20] Lee HT, Chen CT. Numerical and experimental investigation into effect of temperature field on sensitization of AISI 304 in butt welds fabricated by gas tungsten arc welding. *Mater Trans*. 2011;52:1506–1514. Crossref.

[21] Zhou R, Liu Y, Liu B, et al. Precipitation behavior of selective laser melted $FeCoCrNiC_{0.05}$ high entropy alloy. *Intermetallics*. 2019;106:20–25. Crossref.

[22] Wang YM, Voisin T, Mckeown T, et al. Additively manufactured hierarchical stainless steels with high strength and ductility. *Nat Mater*. 2018;17:63–70. Crossref. PubMed.

[23] Otto F, Dlouhý A, Somsen C, et al. The influences of temperature and microstructure on the tensile properties of a CoCrFeMnNi high-entropy alloy. *Acta Mater*. 2013;61:5743–5755. Crossref.

[24] Chen J, Yao Z, Wang X, et al. Effect of C content on microstructure and tensile properties of as-cast CoCrFeMnNi high entropy alloy. *Mater Chem Phys*. 2018;210:136–145. Crossref.

[25] Yim D, Sathiyamoorthi P, Hong SJ, et al. Fabrication and mechanical properties of TiC reinforced CoCrFeMnNi high-entropy alloy composite by water atomization and spark plasma sintering. *J Alloys Compd*. 2019;781:389–396. Crossref.

[26] Laplanche G, Gadaud P, Horst O, et al. Temperature dependencies of the elastic moduli and thermal expansion coefficient of an equiatomic, single-phase CoCrFeMnNi high-entropy alloy. *J Alloys Compd*. 2015;623:348–353. Crossref.

[27] Ungár T, Mecking H. Physics and phenomenology of strain hardening: the FCC case. *Prog Mater Sci*. 2003;48:171–273. Crossref.